Chaos, Solitons and Fractals 208 (2026) 118220

Contents lists available at ScienceDirect

Chaos, Solitons and Fractals

journal homepage: www.elsevier.com/locate/chaos

Topological edge solitons in dislocated extended photonic Lieb lattices

Yanan Ma [a], Hongguang Wang [a], Milivoj R. Belić [b], Dumitru Mihalache [c], Yongdong Li [a], Yiqi Zhang [a,d,*]

[a] Key Laboratory for Physical Electronics and Devices of the Ministry of Education, School of Electronic Science and Engineering, Xi'an Jiaotong University, Xi'an 710049, China

[b] College of Science and Engineering, Hamad Bin Khalifa University, 23874 Doha, Qatar

[c] Horia Hulubei National Institute of Physics and Nuclear Engineering, 077125 Magurele, Bucharest, Romania

[d] State Key Laboratory of Human–Machine Hybrid Augmented Intelligence, Institute of Artificial Intelligence and Robotics, Xi'an Jiaotong University, Xi'an 710049, China

ARTICLE INFO

Keywords:
Topological edge solitons
Lieb lattices
Dislocations
Floquet topological insulators

ABSTRACT

The Lieb lattice is notable for its unique band structure, which features a bosonic-like Dirac cone with flat band crossing the singularity point. It has found applications in a variety of physical fields, including condensed matter physics, optics, acoustics, and cold atomic systems. Extension and dislocation of the regular Lieb lattice introduce new properties and possibilities for generating topological edge states, particularly when the lattice is modulated by a Floquet mechanism mimicked by helical waveguide arrays. Here, we report both bright and dark topological edge solitons in helical dislocated extended Lieb waveguide arrays, which exhibit bearded, pointy, and solid boundaries. The topological edge states on different boundaries display distinct dispersion relations, resulting in either bright or dark solitons. This work provides a promising platform for manipulating the localization of topological objects, and the results offer potential applications in fabricating all-optical functional devices.

1. Introduction

For some time, helical waveguide arrays have been used to mimic Chern insulators [1–3], as the helicity introduces a gauge field [4–6] that breaks the "time"-reversal symmetry of the system, leading to a topological phase transition. Topological insulators based on longitudinally modulated waveguide arrays — not limited to helical ones — are called Floquet topological insulators [7–16], since the longitudinally periodic modulation is equivalent to the Floquet mechanism in condensed matter physics [4,17–20]. Floquet engineering has significantly advanced the field of topological photonics [21–25], giving rise to distinct subfields such as nonlinear topological photonics [26,27], quantum topological photonics [28,29], and non-Hermitian topological photonics [30–34].

Unlike the honeycomb lattice, the Lieb lattice [35] is exceptional for its flat bands [36–42], which are important for beam localization and the exploration of strong correlations [43,44]. In addition to the regular Lieb lattice, extended Lieb lattices have also been created [45–47], which can possess fascinating flat bands or Dirac cones. Floquet topological insulators based on the Lieb lattice [48,49] and its extended versions [50,51] have been theoretically investigated, but have thus far been limited to the linear regime only. Nonlinearity, a mechanism readily accessible in optical platforms, provides a paradigm-shifting perspective on

* Corresponding author.
E-mail address: zhangyiqi@xjtu.edu.cn (Y. Zhang).

https://doi.org/10.1016/j.chaos.2026.118220
Received 31 January 2026; Received in revised form 8 March 2026; Accepted 9 March 2026

topological photonics [26,27] enabling the manipulation of edge state localization, harmonic generation, and anomalous transport, among other phenomena.

In this work, we investigate the topological edge solitons in a helically-extended Lieb waveguide array in its dislocated form. The introduction of a dislocation modifies the lattice symmetry, which generally does not alter the number of sites in the unit cell, leading to the emergence of novel phenomena that supersede the original characteristics of the pristine lattice [52]. A step-by-step analysis of the formation of topological edge solitons is presented. The results demonstrate that the dislocated extended Lieb lattice can serve as a promising platform for manipulating spatial light localization via the interplay among nonlinearity, topology, and dislocation.

2. Results

This section introduces the model considered and presents the results obtained. It is divided into a number of subsections.

2.1. Theoretical model

The propagation of a light beam in optical waveguide arrays with a shallow transverse landscape, fabricated in a transparent dielectric medium, is described by the scaled Schrödinger-like paraxial wave equation

$$i\frac{\partial\psi}{\partial z} = -\frac{1}{2}\nabla^2\psi - \mathcal{R}(x,y,z)\psi - \sigma|\psi|^2\psi, \tag{1}$$

where ψ is the amplitude of the light beam, $\nabla^2 = \partial_x^2 + \partial_y^2$ is the transverse Laplacian, x and y denote the normalized transverse coordinates and z is the longitudinal coordinate. The function $\mathcal{R}(x,y,z)$ describes the waveguide array, with its transverse landscape exhibiting the lattice defined by Gaussian functions

$$\mathcal{R}(x,y,z) = p\sum_{m,n}\exp\left(-\frac{x'^2+y'^2}{w^2}\right), \tag{2}$$

where $p = 8$ represents the depth of the potential, $w = 0.5$ is the site width, and

$$\begin{aligned} x' &= x - x_{m,n} - r\sin(\omega z),\\ y' &= y - y_{m,n} - r\cos(\omega z) + r,\\ z' &= z, \end{aligned}$$

describe a helical waveguide array [1], with helical radius r, helical period $\mathrm{Z} = 2\pi/\omega$, and $(x_{m,n}, y_{m,n})$ denoting the lattice site coordinates at $z = 0$. In Eq. (1), $\sigma = \pm 1$ determines the type of system nonlinearity, which is focusing for $\sigma = +1$ and defocusing for $\sigma = -1$.

Experimentally, helical waveguide arrays can be fabricated in fused silica using the femtosecond laser direct-writing technique [1,12,53–58]. The following estimates appear realistic. For a probing beam wavelength of $\lambda = 800$ nm, a characteristic beam width of $r_0 = 10$ μm, and a lattice constant $a = 2$ corresponding to 20 μm, the Rayleigh length is $R_d = kr_0^2 \approx 1.14$ mm with $k = 2\pi n_0/\lambda$, and $p = 8$ corresponds to a refractive index change of $\delta n = n_0 p/(k^2 r_0^2) \approx 9.0\times 10^{-4}$. The real field amplitude E is related to the dimensionless field ψ by

$$E = \sqrt{\frac{n_0}{k^2 r_0^2 n_2}}\psi$$

with $n_2 \approx 2.7\times 10^{-20}$ m^2/W being the nonlinear refractive index coefficient.

Applying the slowly-varying envelope approximation and the adiabatic approximation, the solution of Eq. (1) can be written as

$$\psi(x,y,z) = u(x,y,z)\exp(ibz), \tag{3}$$

where $u(x,y,z)$ is the envelope of the light beam and b is the corresponding propagation constant. Substituting Eq. (3) into Eq. (1) yields

$$bu = i\frac{\partial u}{\partial z} + \frac{1}{2}\nabla^2 u + \mathcal{R}(x,y,z)u + \sigma|u|^2 u, \tag{4}$$

which constitutes an eigenvalue problem.

2.2. Straight photonic Lieb lattices and band structures

We consider an extended Lieb lattice and its dislocated pair, as displayed in Fig. 1(a) and (b). In the former lattice, there are four sites in the unit cell, which is illustrated by a dashed rectangle. In the dislocated Lieb lattice, the unit cell is no longer a rectangle but a rhombus, which still has four sites, as indicated by the dashed rhombus in Fig. 1(b). Since the waveguide array is straight, Eq. (4) can be rewritten as

$$bu = \frac{1}{2}\nabla^2 u + \mathcal{R}(x,y)u + \sigma|u|^2 u. \tag{5}$$

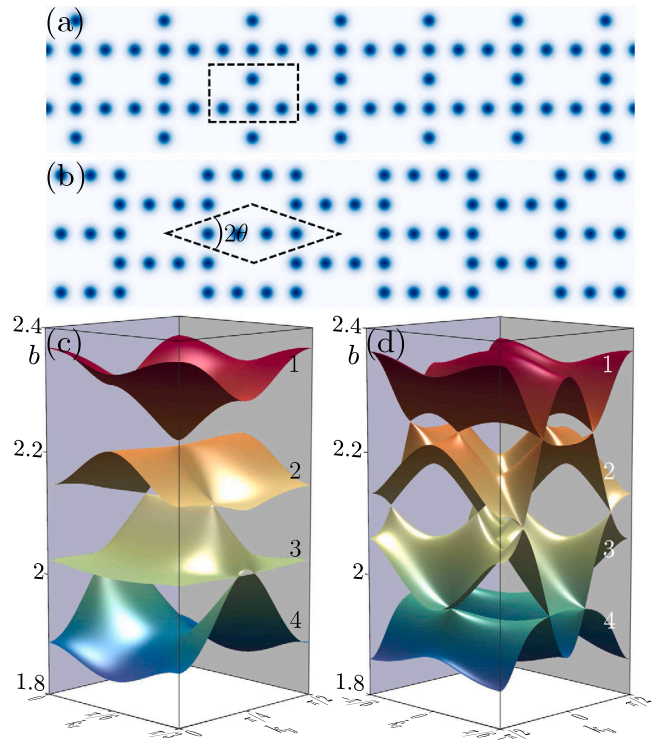

Fig. 1. (a) Extended photonic Lieb lattice. (b) Dislocated extended photonic Lieb lattice. (c,d) Band structures corresponding to lattices in (a,b). Dashed geometric shapes in (a,b) represent the unit cells. (For interpretation of the references to colour in this figure legend, the reader is referred to the web version of this article.)

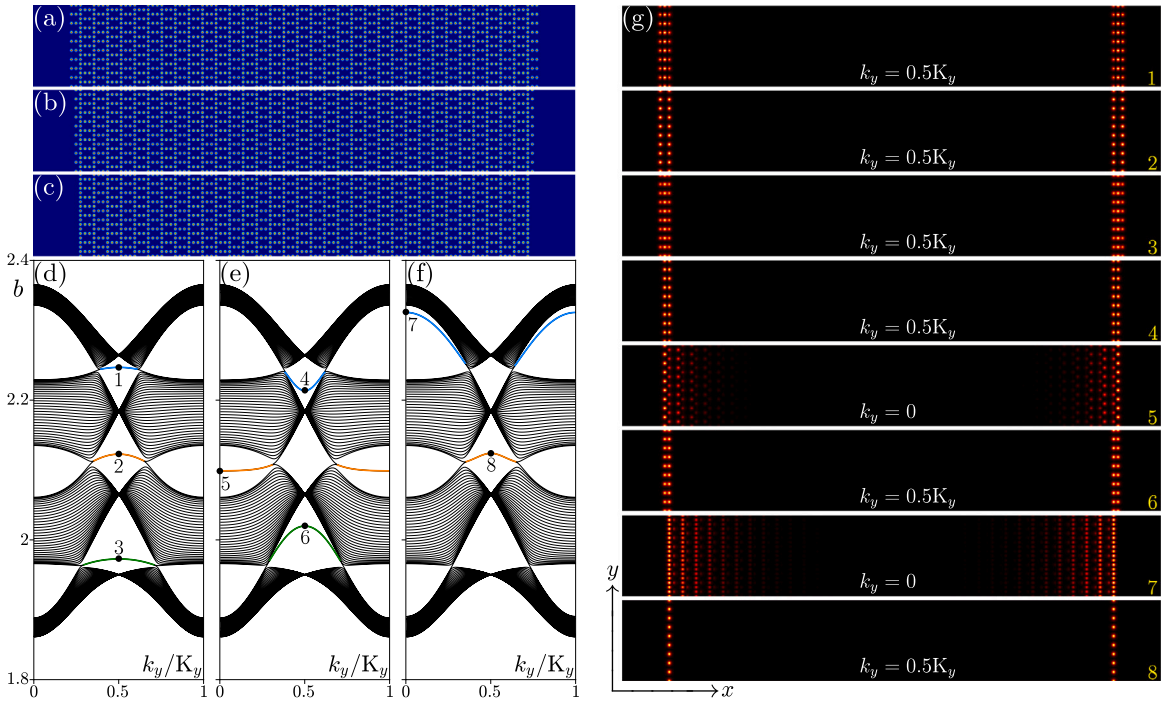

Fig. 2. (a–c) Photonic Lieb lattices of bearded-bearded type, pointy-pointy type, and solid–solid type boundaries, respectively. (d–f) Band structures corresponding to the lattices in (a–c). The black curves are the bulk states, while the colored curves are the edge states. (g) Modulus profiles of the selected edge states numbered in (d–f). (For interpretation of the references to colour in this figure legend, the reader is referred to the web version of this article.)

Neglecting the nonlinear term in Eq. (5), the band structure of the lattices, i.e., the relation between the propagation constant b and the Bloch momenta $k_{x,y}$, can be obtained using the plane-wave expansion method. The band structure of the extended Lieb lattice in Fig. 1(a) is displayed in Fig. 1(c), exhibiting type-III Dirac cones [59], which is distinct from the band structure of the conventional Lieb lattice [36,37]. Note that the Lieb lattice in Fig. 1(a) is not regular but an extended one, so there is neither flat band nor Dirac cone in the band structure in Fig. 1(c).

Calculating the band structure of the lattice in Fig. 1(b) is less straightforward, because its unit cell is rhombic rather than rectangular. To proceed, it is convenient to deform the rhombic unit cell in Fig. 1(b) into a square one. We first rotate the lattice anticlockwise by an angle $\theta = \arctan(1/3)$ into the frame (x_r, y_r, z_r), via

$$\begin{bmatrix} x_r \\ y_r \\ z_r \end{bmatrix} = \begin{bmatrix} \cos(\theta) & -\sin(\theta) & 0 \\ \sin(\theta) & \cos(\theta) & 0 \\ 0 & 0 & 1 \end{bmatrix} \begin{bmatrix} x \\ y \\ z \end{bmatrix}, \tag{6}$$

and then deform the lattice to the frame (x_d, y_d, z_d), via

$$\begin{bmatrix} x_d \\ y_d \\ z_d \end{bmatrix} = \frac{1}{\sin(2\theta)} \begin{bmatrix} \sin(2\theta) & -\cos(2\theta) & 0 \\ 0 & 1 & 0 \\ 0 & 0 & \sin(2\theta) \end{bmatrix} \begin{bmatrix} x_r \\ y_r \\ z_r \end{bmatrix}. \tag{7}$$

After these transformations, Eqs. (1) and (5) become

$$i\frac{\partial \psi_d}{\partial z_d} = -\frac{1}{2\sin^2(2\theta)} \left(\frac{\partial^2}{\partial x_d^2} + \frac{\partial^2}{\partial y_d^2} - 2\cos(2\theta)\frac{\partial^2}{\partial x_d \partial y_d} \right) \psi_d - \mathcal{R}(x_d, y_d, z_d)\psi_d - \sigma|\psi_d|^2\psi_d, \tag{8}$$

and

$$bu_d = \frac{1}{2\sin^2(2\theta)} \left(\frac{\partial^2}{\partial x_d^2} + \frac{\partial^2}{\partial y_d^2} - 2\cos(2\theta)\frac{\partial^2}{\partial x_d \partial y_d} \right) u_d + \mathcal{R}(x_d, y_d)u_d + \sigma|u_d|^2 u_d, \tag{9}$$

where ψ_d and u_d are the amplitude and envelope in the deformed frame. Using the phase factor

$$\exp[i(k_x^d x_d + k_y^d y_d)]$$

and after some algebra, the Bloch momenta in the deformed frame (k_x^d, k_y^d) become related to those in the original frame (k_x, k_y) by

$$\begin{bmatrix} k_x \\ k_y \end{bmatrix} = \frac{1}{\sin(2\theta)} \begin{bmatrix} \sin(\theta) & \sin(\theta) \\ -\cos(\theta) & \cos(\theta) \end{bmatrix} \begin{bmatrix} k_x^d \\ k_y^d \end{bmatrix}. \tag{10}$$

Based on Eqs. (8)–(10), the band structure of the dislocated extended Lieb lattice in Fig. 1(b) is obtained, as shown in Fig. 1(d), possessing useful Dirac cones. It is worth noting that the corresponding asymmetric conical diffraction patterns have already been predicted [60]. In this work, we focus on this dislocated extended Lieb lattice and refer to it simply as the Lieb lattice hereafter.

The Lieb lattice in Fig. 1(b) exhibits a variety of boundary types, including the bearded boundary, the pointy boundary, and the solid boundary, as shown in Fig. 2(a)–(c), respectively. The lattice ribbons in Fig. 2 are periodic in the y direction, so only the Bloch momentum k_y is well defined. The corresponding band structures, i.e., the relations between b and k_y, are illustrated in Fig. 2(d)–(f), where $\mathrm{K}_y = 2\pi/\mathrm{Y}$ and $\mathrm{Y} = 2a$. The Brillouin zone is $-0.5\mathrm{K}_y \le k_y \le 0.5\mathrm{K}_y$ and is periodic, with K_y being the period. Thus, $k_y = 0.5\mathrm{K}_y$ marks the boundary of the Brillouin zone and $k_y = \mathrm{K}_y$ (overlapping with $k_y = 0$) is its center.

Edge states exist in the band structure regardless of which boundary type is adopted. For the bearded boundary, edge states are concentrated around $k_y = 0.5\mathrm{K}_y$, as highlighted by the blue, orange, and green lines in Fig. 2(d). For the pointy boundary, edge states in Fig. 2(e) appear both around $k_y = 0.5\mathrm{K}_y$ (blue and orange curves) and at the center of the Brillouin zone (the green curve). For the solid boundary, edge states indicated by the blue curves reside mainly at the Brillouin zone center, as shown in Fig. 2(f). The green edge state, located near the Brillouin zone boundary, resembles that of the bearded case in Fig. 2(d). We select edge states marked with numbers from Fig. 2(d)–(f), taken either at the boundary or in the center of the Brillouin zone, and display their modulus profiles in Fig. 2(g). These edge states are well localized at the boundaries, except for the state numbered 7, which lies close to the bulk band and considerably penetrates into the bulk.

2.3. Helical photonic Lieb lattices and band structures

The helical waveguide array is frequently employed to break the system's effective time-reversal symmetry, as it generates a gauge field [6]. This becomes evident if the system is transformed from the original frame to the helical frame, when Eq. (1) becomes

$$i\frac{\partial \psi}{\partial z'} = -\frac{1}{2}\nabla'^2\psi - \mathcal{R}(x', y')\psi - \sigma|\psi|^2\psi + ir\omega\left(\cos(\omega z')\frac{\partial \psi}{\partial x'} - \sin(\omega z')\frac{\partial \psi}{\partial y'}\right). \tag{11}$$

By defining $\boldsymbol{A} = r\omega[-\cos(\omega z'), \sin(\omega z')]$, Eq. (11) can be recast as

$$i\frac{\partial \psi}{\partial z'} = -\frac{1}{2}(\nabla' + i\boldsymbol{A})^2\psi - \frac{1}{2}r^2\omega^2\psi - \mathcal{R}(x', y')\psi - \sigma|\psi|^2\psi. \tag{12}$$

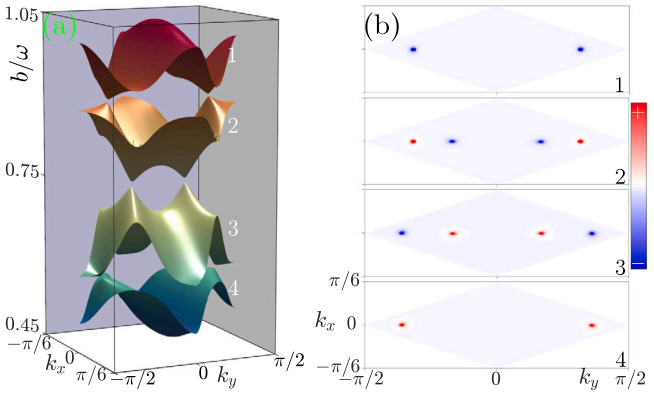

Fig. 3. (a) Quasi-propagation constant b of the helical waveguide array. (b) Berry curvatures of the bands in (a). Parameters are: $p = 8$, $w = 0.5$, $r = 0.4$, Z = 8, and $a = 2$. (For interpretation of the references to colour in this figure legend, the reader is referred to the web version of this article.)

Now, $\boldsymbol{A}$ acts as a vector potential in electromagnetism, associated with a spatially homogeneous electric field of circular polarization [21,22,61], given by

$$\boldsymbol{\mathcal{E}}(z') = -\frac{d\boldsymbol{A}}{dz'} = -r\omega^2[\sin(\omega z'), \cos(\omega z')].$$

We emphasize that the propagation distance z in Eq. (1), as well as z' in Eq. (11), are equivalent to the evolution time "t", so that the curl of $\boldsymbol{A}$ vanishes: $\nabla \times \boldsymbol{A}(t) = 0$, indicating the absence of an effective magnetic field. The band structure of the helically extended Lieb waveguide array — the quasi-propagation constant b versus Bloch momenta $k_{x,y}$ — is displayed in Fig. 3(a), corresponding to the band structure in Fig. 1(d) As anticipated, the Dirac cones vanish due to the array's helicity. The Berry curvature [62,63] of the nth band is expressed as

$$\mathcal{B}_n(\boldsymbol{k}) = i \sum_{n' \neq n} \left(\frac{\langle u_n|\partial_{k_x}\mathcal{H}|u_{n'}\rangle\langle u_{n'}|\partial_{k_y}\mathcal{H}|u_n\rangle}{(b_n - b_{n'})^2} - \frac{\langle u_n|\partial_{k_y}\mathcal{H}|u_{n'}\rangle\langle u_{n'}|\partial_{k_x}\mathcal{H}|u_n\rangle}{(b_n - b_{n'})^2} \right), \tag{13}$$

where $|u_n\rangle$ and b_n denote the eigenstates and eigenvalues of the system's linear Hamiltonian $\mathcal{H}$, and $\langle\cdot|\cdot\rangle$ is the inner product. The distributions $\mathcal{B}_n(\boldsymbol{k})$ for bands $n = 1 \sim 4$ are presented in Fig. 3(b). Note that the Berry curvature is plotted within the first Brillouin zone (BZ), which takes the form of a rhombus (or hexagon). The topological index characterizing this system is given by the Chern number [63–66] in the first BZ:

$$C_{n,\mathrm{BZ}} = \frac{1}{2\pi}\int_{\mathrm{BZ}} \mathcal{B}_n(\boldsymbol{k})d\boldsymbol{k}, \tag{14}$$

where BZ indicates that the integration is carried over the entire Brillouin zone. Corresponding to the Berry curvatures presented in Fig. 3(b), the Chern numbers for bands $1 \sim 4$ are $C_1 = 1$, $C_2 = 0$, $C_3 = 0$, and $C_4 = -1$, respectively. According to the bulk-edge correspondence principle [22], a topological edge state is expected to appear within each band gap in Fig. 3(a) when the lattice is subjected to open boundary conditions.

2.4. Topological edge solitons

Corresponding to the boundary types of helical waveguide arrays displayed in the top panels of Fig. 2(a)–(c), we present the helical waveguide arrays and their band structures (i.e., the quasi-propagation constant b versus the Bloch momentum k_y) in Fig. 4(a)–(c). As predicted, the originally degenerate edge states in each band gap become non-degenerate and have opposite slopes. For the bearded-bearded boundary in Fig. 4(a), all pairs of topological edge states resemble those of the helical honeycomb waveguide array [1]. However, for the pointy-pointy boundary in Fig. 4(b) and the solid–solid boundary in Fig. 4(c), the topological edge states in the top and bottom band gaps lie close to the bulk bands and are similar to those in lattices with type-II Dirac cones [67–69]. We are interested in the topological edge states in the middle band gap, which are highlighted in red and blue. Several topological edge states ϕ_{k_y}, indicated by the numbered dots in Fig. 4(a)–(c), are selected, and their modulus profiles are displayed in Fig. 4(d). We find that the topological edge states from the blue curve reside on the left boundary, whereas those from the red curve reside on the right boundary of the waveguide array.

The variety of topological edge states in the dislocated Lieb lattice provides an opportunity for exploring different topological edge solitons [70–75]. Assuming that the first-order derivative of the edge state $b' = db/dk_y$ determines its group velocity $v = -b'$ and the second-order derivative $b'' = d^2b/dk_y^2$ determines its dispersion, we show those two quantities in Fig. 5(a)–(c), corresponding to the red and blue curves from Fig. 4(a)–(c).

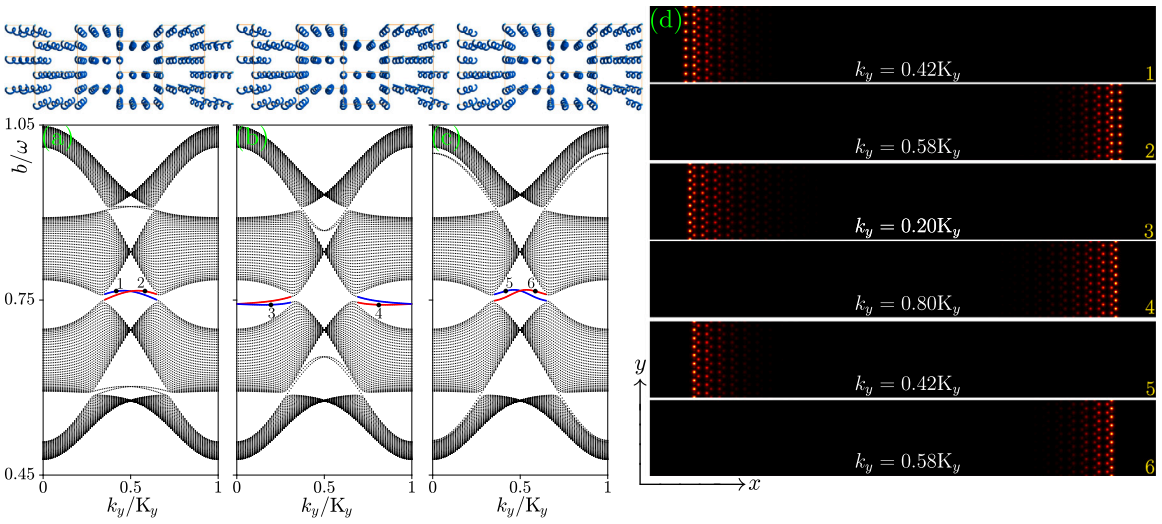

Fig. 4. (a–c) Band structures of the helical waveguide arrays with different boundary types that are displayed on top of the bands. (d) Modulus profiles of the numbered topological edge states. Parameters are the same as those in Fig. 3. (For interpretation of the references to colour in this figure legend, the reader is referred to the web version of this article.)

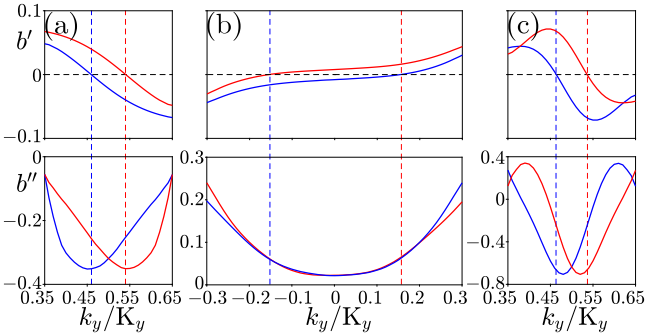

Fig. 5. First-order derivative $b' = db/dk_y$ (a–c) and second-order derivative $b'' = d^2b/dk_y^2$ (d–f) of the topological edge states indicated by red and blue lines in Fig. 4(a–c). (For interpretation of the references to colour in this figure legend, the reader is referred to the web version of this article.)

In Fig. 5(a), the two edge states move in opposite directions along the boundary of the helical waveguide array, when their Bloch momenta lie between the vertical dashed lines; otherwise they propagate in the same direction. Since b'' is always negative in the existence regions of edge states, the bright edge solitons along the bearded-bearded boundary can form, depending on their linear counterparts. For the case shown in Fig. 5(b), dark edge solitons along the pointy-pointy boundary can be predicted, since b'' is always positive. The case shown in Fig. 5(c) displays both positive and negative b'' in the existence region; however, positive b'' occurs only near the region where the edge state approaches the bulk band, which induces coupling between the edge state and bulk states and consequently, reduces the localization of the edge state. Therefore, we expect bright edge solitons along the solid–solid boundary.

To construct an edge soliton, we superimpose a soliton envelope on the linear Floquet edge state $\phi_{k_y}(x, y, z)$, as $\psi(x, y, z) = \mathcal{A}(\eta, z)\phi_{k_y}(x, y, z)\exp(ibz)$. Inserting this ansatz into Eq. (1) and after some algebra, the slowly-varying envelope $\mathcal{A}(y)$ is found to obey the following equation [70]

$$i\frac{\partial \mathcal{A}}{\partial z} = \frac{b''}{2}\frac{\partial^2 \mathcal{A}}{\partial^2 \eta} - \chi|\mathcal{A}|^2\mathcal{A}, \tag{15}$$

where

$$\chi = \frac{1}{\mathrm{Z}}\int_0^{\mathrm{Z}} dz \int_{-\infty}^{+\infty} dx \int_0^{\mathrm{Y}} |\phi_{k_y}(x, y, z)|^4 dy$$

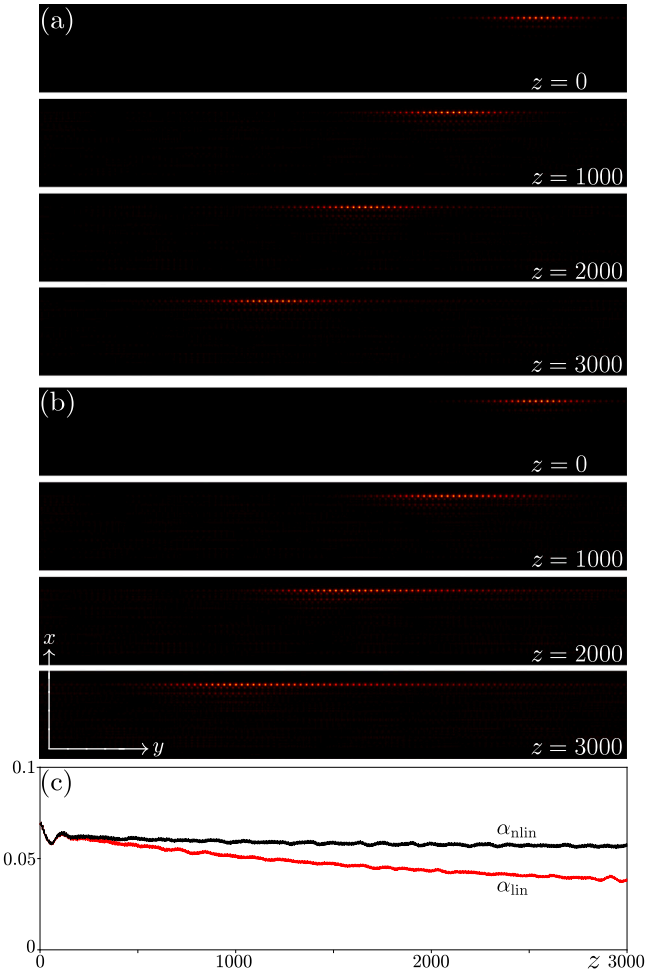

Fig. 6. (a) Modulus profiles of the bright edge soliton with $k_y = 0.48\mathrm{K}_y$ at selected distances in the helical waveguide array shown in Fig. 4(c). (b) Same setup as in (a), but with the nonlinear term removed. (c) Peak amplitude of the bright edge soliton and its linear counterpart. (For interpretation of the references to colour in this figure legend, the reader is referred to the web version of this article.)

and $\eta = y + b'z$. The solutions of this simple cubic nonlinear Schrödinger Eq. (15) are well-known and include the bright pulse

$$\mathcal{A}(y) = \sqrt{2\frac{b_{\mathrm{nl}}}{\chi}}\,\mathrm{sech}\left(\eta\sqrt{-2\frac{b_{\mathrm{nl}}}{b''}}\right)\exp\left(ib_{\mathrm{nl}}z\right), \tag{16}$$

and the dark pulse

$$\mathcal{A}(y) = \sqrt{\frac{b_{\mathrm{nl}}}{\chi}}\,\tanh\left(\eta\sqrt{\frac{b_{\mathrm{nl}}}{b''}}\right)\exp\left(ib_{\mathrm{nl}}z\right), \tag{17}$$

Here, b_{nl} is the propagation constant detuning, which should not be too large for stable solutions. The solutions in Eqs. (16) and (17) feature bright and dark envelopes, respectively. From these, we construct bright and dark edge solitons, displayed in Figs. 6 and 7, respectively.

The bright soliton maintains its profile during unidirectional propagation in the negative y direction, as shown in Fig. 6(a). If the nonlinearity is removed, it spreads quickly during propagation and gradually fills the extent of the lattice, as exhibited in Fig. 6(b). One can compare the modulus profile of the same input at different propagation distances. We also record the peak amplitudes α_{lin} and α_{nlin} of the beam during linear and nonlinear propagation, indicated by the red and black curves in Fig. 6(c). Notably, the black curve illustrates that the peak amplitude of the bright soliton remains constant during propagation, whereas the red curve indicates a decreasing peak amplitude with increasing propagation distance. Note that the potential excitation energy of the edge state soliton shown in Fig. 6(a) is ~1.16 nJ if the laser pulse duration is 100 fs, which is feasible in experiment.

The dark edge soliton, represented by two notches in Fig. 7(a), also maintains its profile during unidirectional propagation, as seen in the panel at $z = 2000$ of Fig. 7(a). However, the profile is not preserved during linear propagation, as shown in Fig.

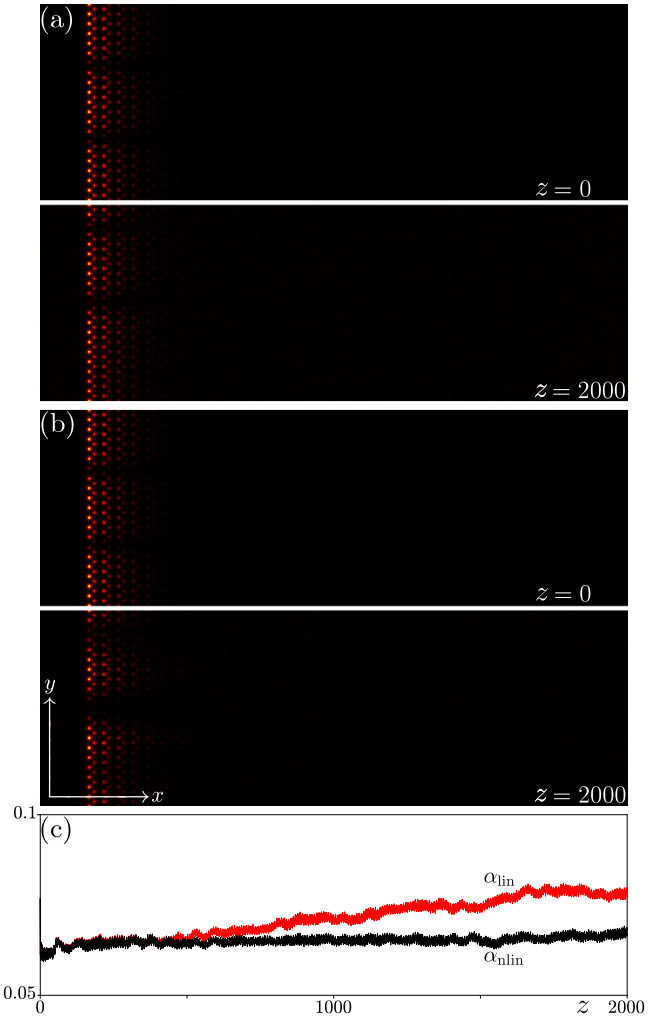

Fig. 7. Same as Fig. 6 but for the dark edge soliton with $k_y = 0.01\mathrm{K}_y$ in the helical waveguide array shown in Fig. 4(b). (For interpretation of the references to colour in this figure legend, the reader is referred to the web version of this article.)

7(b). The width of the notches broadens, and the peak of the bright sectors increases. The comparison between linear and nonlinear propagation reveals a pronounced difference in peak amplitudes, as exhibited in Fig. 7(c). As seen, the peak amplitude during linear propagation (the red curve) increases with distance, while that of nonlinear propagation (the black curve) maintains its value.

Figs. 6 and 7 demonstrate topological edge solitons in the Floquet modulated extended Lieb waveguide array. More types of topological edge solitons are expected in this model, such as vector topological edge solitons [68,76,77] because additional topological edge states are observed in Fig. 4(a)–(c), chiral bulk solitons [78], and nonlinear corner states [53,79–81]. It is worth stressing that bending losses are inevitable in helical waveguide arrays, so the radius should not be too large and the period should not be too small. According to our numerical simulations, the bending loss is not too strong to lead to quick decay of the edge state soliton if the radius is smaller than $r = 0.6$ with other parameters unchanged. The parameters provided in this work are reasonable and can serve as a reference for future experiments.

3. Conclusion and outlook

In summary, we have reported bright and dark topological edge solitons in helical dislocated extended Lieb waveguide arrays, which possess various boundary types. The topological edge states may appear around either the middle or at the boundary of the first Brillouin zone, and may support either bright or dark topological edge solitons, depending on the boundary type. We provide a versatile lattice platform for investigating the localization of topological fields, which may also support vector topological edge states.

To the best of our knowledge, the experimental observation of real topological edge solitons is still an open and ready-to-explore topic, although some relevant experiments have been performed [82–84]. Potential experimental systems to be employed include

femtosecond-laser-written waveguide arrays [25,58,85,86], as well as waveguide arrays induced in photorefractive crystals [67] or atomic vapors [87].

CRediT authorship contribution statement

Yanan Ma: Investigation, Formal analysis, Data curation. **Hongguang Wang:** Supervision. **Milivoj R. Belić:** Writing – review & editing, Supervision. **Dumitru Mihalache:** Writing – review & editing, Supervision. **Yongdong Li:** Supervision. **Yiqi Zhang:** Writing – review & editing, Supervision, Investigation, Funding acquisition, Formal analysis, Conceptualization.

Funding

This work was supported by the Natural Science Basic Research Program of Shaanxi Province (2024JC-JCQN-06, 2025JC-QYCX-006), and the National Natural Science Foundation of China (12474337), and Sichuan Science and Technology Program (2025ZNSFSC1458).

Declaration of competing interest

The authors declare that they have no known competing financial interests or personal relationships that could have appeared to influence the work reported in this paper.

Data availability

Data will be made available on request.

References

[1] Rechtsman MC, Zeuner JM, Plotnik Y, Lumer Y, Podolsky D, Dreisow F, et al. Photonic floquet topological insulators. Nature 2013;496:196–200.
[2] Ablowitz MJ, Cole JT. Tight-binding methods for general longitudinally driven photonic lattices: Edge states and solitons. Phys Rev A 2017;96:043868.
[3] Zhong H, Wang R, Ye F, Zhang J, Zhang L, Zhang YP, et al. Topological insulator properties of photonic kagome helical waveguide arrays. Results Phys 2019;12:996–1001.
[4] Rudner MS, Lindner NH. Band structure engineering and non-equilibrium dynamics in floquet topological insulators. Nat Rev Phys 2020;2(5):229–44.
[5] Yin S, Galiffi E, Alù A. Floquet metamaterials. ELight 2022;2(1):8.
[6] Song W, Yang Y, Lin Z, Liu X, Wu S, Chen C, et al. Artificial gauge fields in photonics. Nat Rev Phys 2025;7(11):606–20.
[7] Maczewsky LJ, Zeuner JM, Nolte S, Szameit A. Observation of photonic anomalous floquet topological insulators. Nat Commun 2017;8:13756.
[8] Mukherjee S, Spracklen A, Valiente M, Andersson E, Öhberg P, Goldman N, et al. Experimental observation of anomalous topological edge modes in a slowly driven photonic lattice. Nat Commun 2017;8:13918.
[9] Zhang Y, Kartashov YV, Li F, Zhang Z, Zhang Y, Belić MR, et al. Edge states in dynamical superlattices. ACS Photon 2017;4(9):2250–6.
[10] Ivanov SK, Zhang YQ, Kartashov YV, Skryabin DV. Floquet topological insulator laser. APL Photon 2019;4(12):126101.
[11] Zhong H, Kartashov YV, Li Y, Zhang Y. π-Mode solitons in photonic Floquet lattices. Phys Rev A 2023;107:L021502.
[12] Arkhipova AA, Zhang Y, Kartashov YV, Zhuravitskii SA, Skryabin NN, Dyakonov IV, et al. Observation of π solitons in oscillating waveguide arrays. Sci Bull 2023;68(18):2017–24.
[13] Pyrialakos GG, Beck J, Heinrich M, Maczewsky LJ, Kantartzis NV, Khajavikhan M, et al. Bimorphic Floquet topological insulators. Nat Mater 2022;21(6):634–9.
[14] Ren B, Kartashov YV, Wang H, Li Y, Zhang Y. Floquet topological insulators with hybrid edges. Chaos Solitons Fractals 2023;166:113010.
[15] Shen S, Kartashov YV, Li Y, Zhang Y. Floquet edge solitons in modulated trimer waveguide arrays. Phys Rev Appl 2023;20:014012.
[16] Shen S, Kartashov YV, Li Y, Cao M, Zhang Y. π mode lasing in the non-Hermitian Floquet topological system. APL Photon 2024;9(8):086113.
[17] Kitagawa T, Berg E, Rudner M, Demler E. Topological characterization of periodically driven quantum systems. Phys Rev B 2010;82:235114.
[18] Lindner NH, Refael G, Galitski V. Floquet topological insulator in semiconductor quantum wells. Nat Phys 2011;7(6):490–5.
[19] Oka T, Kitamura S. Floquet engineering of quantum materials. Annu Rev Condens Matter Phys 2019;10:387–408.
[20] Bao CH, Fan BS, Tang PZ, Duan WH, Zhou SY. Floquet engineering in quantum materials (in Chinese). Acta Phys Sin 2023;72(23):234202.
[21] Lu L, Joannopoulos JD, Soljačić M. Topological photonics. Nat Photon 2014;8(11):821–9.
[22] Ozawa T, Price HM, Amo A, Goldman N, Hafezi M, Lu L, et al. Topological photonics. Rev Modern Phys 2019;91:015006.
[23] Zhang X, Zangeneh-Nejad F, Chen ZG, Lu MH, Christensen J. A second wave of topological phenomena in photonics and acoustics. Nature 2023;618(7966):687–97.
[24] Lin ZK, Wang Q, Liu Y, Xue H, Zhang B, Chong Y, et al. Topological phenomena at defects in acoustic, photonic and solid-state lattices. Nat Rev Phys 2023;5(8):483–95.
[25] Yan W, Zhang B, Chen F. Photonic topological insulators in femtosecond laser direct-written waveguides. npj Nanophoton 2024;1(1):40.
[26] Smirnova D, Leykam D, Chong Y, Kivshar Y. Nonlinear topological photonics. Appl Phys Rev 2020;7(2):021306.
[27] Szameit A, Rechtsman MC. Discrete nonlinear topological photonics. Nat Phys 2024;20(6):905–12.
[28] Yan Q, Hu X, Fu Y, Lu C, Fan C, Liu Q, et al. Quantum topological photonics. Adv Opt Mater 2021;9(15):2001739.
[29] Hashemi A, Zakeri MJ, Jung PS, Blanco-Redondo A. Topological quantum photonics. APL Photon 2025;10(1):010903.
[30] Ota Y, Takata K, Ozawa T, Amo A, Jia Z, Kante B, et al. Active topological photonics. Nanophoton 2020;9(3):547–67.
[31] Parto M, Liu YGN, Bahari B, Khajavikhan M, Christodoulides DN. Non-hermitian and topological photonics: optics at an exceptional point. Nanophoton 2021;10(1):403–23.
[32] Yan Q, Zhao B, Zhou R, Ma R, Lyu Q, Chu S, et al. Advances and applications on non-Hermitian topological photonics. Nanophoton 2023;12(13):2247–71.
[33] Nasari H, Pyrialakos GG, Christodoulides DN, Khajavikhan M. Non-Hermitian topological photonics. Opt Mater Express 2023;13(4):870–85.
[34] Chen S, Basit A, Li L, Hou C, Ruan Y, Wei Y, et al. Non-Hermitian topological lattice photonics: An analytic perspective. Adv Photon Res 2025;6(11):2500083.
[35] Lieb EH. Two theorems on the Hubbard model. Phys Rev Lett 1989;62:1201–4.

[36] Vicencio RA, Cantillano C, Morales-Inostroza L, Real B, Mejía-Cortés C, Weimann S, et al. Observation of localized states in Lieb photonic lattices. Phys Rev Lett 2015;114:245503.
[37] Mukherjee S, Spracklen A, Choudhury D, Goldman N, Öhberg P, Andersson E, et al. Observation of a localized flat-band state in a photonic Lieb lattice. Phys Rev Lett 2015;114:245504.
[38] Zhang YQ, Liu X, Belić M, Zhong WP, Li CB, Chen HX, et al. Dispersion relations of strained and complex Lieb lattices based on the tight-binding method. Rom Rep Phys 2016;68:230–40.
[39] Xia S, Hu Y, Song D, Zong Y, Tang L, Chen Z. Demonstration of flat-band image transmission in optically induced Lieb photonic lattices. Opt Lett 2016;41:1435–8.
[40] Xia S, Ramachandran A, Xia S, Li D, Liu X, Tang L, et al. Unconventional flatband line states in photonic Lieb lattices. Phys Rev Lett 2018;121:263902.
[41] Jiang W, Kang M, Huang H, Xu H, Low T, Liu F. Topological band evolution between Lieb and kagome lattices. Phys Rev B 2019;99:125131.
[42] Ding C, Zhu Y, Lu Q, Zhang Z, Shao D, Huang T, et al. Flat-band Lieb electride with emergent quantum phase transitions and superconductivity. Chin Phys Lett 2025;42(11):110709.
[43] Leykam D, Andreanov A, Flach S. Artificial flat band systems: from lattice models to experiments. Adv Phys X 2018;3(1):1473052.
[44] Leykam D, Flach S. Perspective: Photonic flatbands. APL Photon 2018;3(7):070901.
[45] Zhang D, Zhang YQ, Zhong H, Li CB, Zhang ZY, Zhang YP, et al. New edge-centered photonic square lattices with flat bands. Ann Phys 2017;382:160–9.
[46] Bhattacharya A, Pal B. Flat bands and nontrivial topological properties in an extended Lieb lattice. Phys Rev B 2019;100:235145.
[47] Hanafi H, Menz P, McWilliam A, Imbrock J, Denz C. Localized dynamics arising from multiple flat bands in a decorated photonic Lieb lattice. APL Photon 2022;7(11):111301.
[48] Bandres MA, Rechtsman M, Szameit A, Segev M. Lieb photonic topological insulator. In: CLEO: 2014. Optical Society of America; 2014, p. FF2D.3.
[49] Ablowitz MJ, Cole JT. Topological insulators in longitudinally driven waveguides: Lieb and kagome lattices. Phys Rev A 2019;99:033821.
[50] Wichmann JJ, Hanafi H, Lang JP, Denz C. Topological edge transport in a Lieb-like photonic lattice. In: 2021 conference on lasers and electro-optics europe and European quantum electronics conference. Optica Publishing Group; 2021, p. ec_p_22.
[51] Wichmann J, Hanafi H, Imbrock J, Denz C. Rabi-like oscillations in topologically protected edge states of a photonic Floquet topological insulator. In: Optica advanced photonics congress 2022. Optica Publishing Group; 2022, NpM2E.2.
[52] Li C, Ye F, Chen X, Kartashov YV, Ferrando A, Torner L, et al. Lieb polariton topological insulators. Phys Rev B 2018;97:081103.
[53] Kirsch MS, Zhang Y, Kremer M, Maczewsky LJ, Ivanov SK, Kartashov YV, et al. Nonlinear second-order photonic topological insulators. Nat Phys 2021;17(9):995–1000.
[54] Arkhipova AA, Kartashov YV, Ivanov SK, Zhuravitskii SA, Skryabin NN, Dyakonov IV, et al. Observation of linear and nonlinear light localization at the edges of Moiré arrays. Phys Rev Lett 2023;130:083801.
[55] Ren B, Arkhipova AA, Zhang Y, Kartashov YV, Wang H, Zhuravitskii SA, et al. Observation of nonlinear disclination states. Light Sci Appl 2023;12(1):194.
[56] Zhong H, Kompanets VO, Zhang Y, Kartashov YV, Cao M, Li Y, et al. Observation of nonlinear fractal higher order topological insulator. Light Sci Appl 2024;13(1):264.
[57] Kompanets VO, Feng S, Zhang Y, Kartashov YV, Li Y, Zhuravitskii SA, et al. Observation of nonlinear topological corner states originating from different spectral charges. Adv Mater 2025;37(30):2500556.
[58] Wu H, Cheng W, Chen R, Zhang B, Liu X, Yan W, Chen F. Observation of distinct bound states in the continuum in the strained type-II Dirac photonic lattices. J Phys Photon 2026;8(1):015037.
[59] Milićević M, Montambaux G, Ozawa T, Jamadi O, Real B, Sagnes I, et al. Type-III and tilted Dirac cones emerging from flat bands in photonic orbital graphene. Phys Rev X 2019;9:031010.
[60] Zhong H, Wang R, Belić MR, Zhang Y, Zhang Y. Asymmetric conical diffraction in dislocated edge-centered square lattices. Opt Express 2019;27(5):6300–9.
[61] Jackson JD. Classical electrodynamics. John Wiley & Sons; 2021.
[62] Xiao D, Chang MC, Niu Q. Berry phase effects on electronic properties. Rev Modern Phys 2010;82:1959–2007.
[63] Fuchs JN, Piéchon F, Goerbig MO, Montambaux G. Topological Berry phase and semiclassical quantization of cyclotron orbits for two dimensional electrons in coupled band models. Eur Phys J B 2010;77(3):351–62.
[64] Fukui T, Hatsugai Y, Suzuki H. Chern numbers in discretized Brillouin zone: Efficient method of computing (spin) Hall conductances. J Phys Soc Japan 2005;74(6):1674–7.
[65] He C, Zhao L, Zhang S, Zhou L, Ma S. Intrinsic topological hinge states induced by boundary gauge fields in photonic metamaterials. ELight 2025;5(1):19.
[66] Peng R, Yang K, Fu Q, Chen Y, Wang P, Kartashov YV, et al. Topological pumping of light governed by Fibonacci numbers. ELight 2025;5(1):16.
[67] Zhong H, Xia S, Zhang Y, Li Y, Song D, Liu C, et al. Nonlinear topological valley Hall edge states arising from type-II Dirac cones. Adv Photon 2021;3(5):056001.
[68] Tian Y, Zhang Y, Li Y, Belić MR. Vector valley Hall edge solitons in the photonic lattice with type-II Dirac cones. Front Phys (Beijing) 2022;17(5):53503.
[69] Shen S, Belić MR, Zhang Y, Li Y, Wang T, Tian ZN, et al. Edge solitons in non-Hermitian photonic lattices with type-II Dirac cones. Front Phys (Beijing) 2025;20:042203.
[70] Ivanov SK, Kartashov YV, Szameit A, Torner L, Konotop VV. Vector topological edge solitons in floquet insulators. ACS Photon 2020;7(3):735–45.
[71] Ivanov SK, Kartashov YV, Maczewsky LJ, Szameit A, Konotop VV. Edge solitons in Lieb topological floquet insulator. Opt Lett 2020;45(6):1459–62.
[72] Ivanov SK, Kartashov YV, Maczewsky LJ, Szameit A, Konotop VV. Bragg solitons in topological floquet insulators. Opt Lett 2020;45(8):2271–4.
[73] Ivanov SK, Kartashov YV, Heinrich M, Szameit A, Torner L, Konotop VV. Topological dipole floquet solitons. Phys Rev A 2021;103:053507.
[74] Ivanov SK, Kartashov YV, Szameit A, Torner L, Konotop VV. Floquet edge multicolor solitons. Laser Photon Rev 2022;16(3):2100398.
[75] Ivanov SK, Kartashov YV. Floquet valley Hall edge solitons. Chaos Solitons Fractals 2024;186:115239.
[76] Tang Q, Zhang Y, Kartashov YV, Li Y, Konotop VV. Vector valley Hall edge solitons in superhoneycomb lattices. Chaos Solitons Fractals 2022;161:112364.
[77] Tian Y, Wang Y, Belić MR, Zhang Y, Li Y, Ye F. Vector valley Hall edge solitons in distorted type-II Dirac photonic lattices. Opt Express 2023;31(13):20812–24.
[78] Shen S, Shang C, Li Y, Zhang Y. Chiral bulk solitons in photonic graphene with decorated boundaries. Laser Photon Rev 2025;19(3):2401114.
[79] Hu Z, Bongiovanni D, Jukić D, Jajtić E, Xia S, Song D, et al. Nonlinear control of photonic higher-order topological bound states in the continuum. Light Sci Appl 2021;10(1):164.
[80] Zhang Y, Bongiovanni D, Wang Z, Wang X, Xia S, Hu Z, et al. Realization of photonic *p*-orbital higher-order topological insulators. ELight 2023;3(1):5.
[81] Wang Z, Bongiovanni D, Wang X, Hu Z, Jukić D, Song D, et al. Hidden multi-topological phases mediated by constrained inter-cell coupling. ELight 2026;6(1):2.
[82] Maczewsky LJ, Heinrich M, Kremer M, Ivanov SK, Ehrhardt M, Martinez F, et al. Nonlinearity-induced photonic topological insulator. Science 2020;370(6517):701–4.
[83] Mukherjee S, Rechtsman MC. Observation of floquet solitons in a topological bandgap. Science 2020;368(6493):856–9.
[84] Mukherjee S, Rechtsman MC. Observation of unidirectional solitonlike edge states in nonlinear Floquet topological insulators. Phys Rev X 2021;11:041057.
[85] Zhang B, Yan W, Chen F. Recent advances in femtosecond laser direct writing of three-dimensional periodic photonic structures in transparent materials. Adv Photon 2025;7(11):034002.
[86] Lou M, Tan D. Topological insulator: Ultrafast-laser direct-writing engineering and applications (in Chinese). Chin J Lasers 2024;51(4):0402401.
[87] Zhang ZY, Wang R, Zhang YQ, Kartashov YV, Li F, Zhong H, et al. Observation of edge solitons in photonic graphene. Nat Commun 2020;11(1):1902.